Acidity modulation of Pt-supported catalyst enhances C-O bond cleavage over acetone hydrodeoxygenation

Guilherme B. Strapasson [a,b], Leonardo S. Sousa [a], Gabriel B. Báfero [a], Davi S. Leite [a], Beatriz D. Moreno [c], Cristiane B. Rodella [b,*], Daniela Zanchet [a,*]

[a] *Institute of Chemistry, University of Campinas, UNICAMP, Campinas, SP 13083-970, Brazil*
[b] *Brazilian Synchrotron Light Laboratory, CNPEM, Campinas, SP 13083-100, Brazil*
[c] *Canadian Light Source Inc., 44 Innovation Boulevard, Saskatoon, SK S7N 2V3, Canada*

ARTICLE INFO

ABSTRACT

Understanding how to tune the properties of metal oxides, e.g., controlling and manipulating defects and catalytic sites, and establishing a clear understanding of metal support interactions is essential for developing catalysts with enhanced activity, selectivity, and stability. Here, we report the synthesis of Pt-supported Ti-Nb mixed metal oxides, aiming for the acidity modulation of Brønsted and Lewis acid sites of the catalysts' surface. Results demonstrated that the catalyst richer in Brønsted acid sites was a promising candidate for the acetone hydrodeoxygenation reaction, with enhanced stability and preferential selectivity toward C-O bond cleavage during the time on stream. Important insights into the impact of acidity modulation of Pt-supported catalysts were presented here, especially concerning the metal-support interaction. The intrinsic correlation between catalytic sites and reaction mechanism was also discussed.

1. Introduction

Catalyst design and engineering of active sites have helped the development of catalytic systems with unique properties that can be optimized and tuned for various catalytic reactions. The hydrodeoxygenation (HDO) reaction is one of the main biomass-derivate upgrading processes to obtain biofuels, as substitutes for petroleum diesel and gasoline, or platform molecules and specialty chemicals [1]. The HDO reaction is conducted under a hydrogen-rich atmosphere combined with a heterogenous catalyst, leading to oxygen content reduction by selective C-O bond cleavage and generation of hydrocarbons as the main products. Generally, this reaction occurs through a bifunctional mechanism that requires a metallic site for hydrogenation/dehydrogenation and an acid/oxophilic site that adsorbs the oxy- compound and promotes C-O bond activation and dehydration steps [2,3]. However, the reaction network can also encompass other pathways, such as metal-catalyzed demethylations and C-C hydrogenolyses [4]; Brønsted/Lewis acid-catalyzed condensations [5]; and oxygen vacancy-mediated direct deoxygenation [1].

In the case of supported metal catalysts, the metal-support interaction (MSI) can play a critical role in tuning the catalytic behavior. The reactivity, selectivity, and stability of catalysts can be tailored by regulating the MSI at the interface between the metallic phase and the support, and both parts have an essential role in the catalytic reactions [6]. One of the main strategies to tune MSI involves the design of metal/oxide interfaces, which enables significant changes in the electronic structure and geometric configuration of metal species [7,8]. The electronic modulation of the metallic phase can directly impact the catalytic performance, as previously demonstrated for Pt-supported catalysts where size- and shape-controlled Pt nanoparticles carried on various oxide supports (i.e., TiO_2, CeO_2, ZrO_2, Al_2O_3, La_2O_3, and MgO) were explored [8]. They demonstrated that the MSI between Pt and the different oxides led to Pt species with varied electronic profiles, which impacted the selectivity of p-chloronitrobenzene hydrogenation to p-chloroaniline. Such kind of MSI is known as strong metal-support interaction (SMSI), and it has been shown that catalytic systems composed of noble metals supported on specific oxides, e.g., TiO_2 and Nb_2O_5, are favored by the SMSI [9]. For example, SMSI of systems composed of Pt-supported over TiO_2 can occur by three different mechanisms: (i) interfacial charge transfer right at the area of contact between the metal and the support [10]; (ii) evolution of an amorphous TiO_x phase covering the Pt nanoparticle [11]; and lastly (iii)

* Corresponding authors.
E-mail addresses: cristiane.rodella@lnls.br (C.B. Rodella), zanchet@unicamp.br (D. Zanchet).

incorporation of the Pt into TiO$_2$ surface [12].

It is worth highlighting that TiO$_2$-based nanostructured supports have shown high catalytic activity in reduction and oxidation reactions at low temperatures and pressures [13–15]. TiO$_2$ is considered a good support due to its SMSI, chemical stability, redox (with oxygen vacancies creation), and acid-base properties [14]. It is known that coordinatively unsaturated Ti^{4+} sites and Ti-O(H)-Ti bridge bonds on the surface of TiO$_2$-based structures act as Lewis and Brønsted acid sites, respectively [16]. Its acidity, however, is moderate and mostly related to the Lewis type. On the other hand, niobium pentoxide (Nb$_2$O$_5$) is a well-known strong acid catalyst, richer in Brønsted acid sites, which have been applied in several catalytic reactions [16]. The combination of TiO$_2$/Nb$_2$O$_5$ as support, aiming for the acidity modulation between Lewis and Brønsted acid sites, becomes, thus, an attractive option and can represent an efficient way to increase the catalytic activity and acidity of catalysts [17,18]. Furthermore, the bridged hydroxyl groups, Nb-O(H)-Ti, generate strong Brønsted acid sites that can enhance the dehydration capability of the catalyst [19,20]. However, reports on effective Nb addition to the TiO$_2$ matrix, using different synthesis parameters and precursors, are still limited to low loadings ($\leq$ 6 at%) [16, 21,22].

Literature results employing TiO$_2$ as support in the HDO reaction of phenolic compounds showed that the formation of oxophilic sites (Ti$^{3+/4+}$) occured via spillover of H$_2$ activated on the metal (Ru, Pt) and it favored the adsorption of oxygenated molecules at the metal-support interface [23–27]. In the case of SiO$_2$-based catalysts, on the other hand, the interaction was weaker and favored hydrogenation products as it occured predominantly on the metallic sites. In addition to the generation of oxophilic sites, the more reactive nature of TiO$_2$ against SiO$_2$ increased metal dispersion and the creation of interfacial sites. A recent study with Pd/Nb$_2$O$_5$/SiO$_2$ catalysts in phenol HDO showed that the presence of Nb$_2$O$_5$ led to the formation of an oxophilic interface with Pd, increasing the catalytic activity and selectivity to benzene [28]. Pd deposition occurred preferentially on Nb$_2$O$_5$, even with low loadings, demonstrating that the creation of the metal interface sites and their nature seem to be crucial factors in developing efficient catalysts for HDO reactions. However, the correlation between the acidity of the support and its impact on the MSI is still unclear, especially for those supported over metal oxides.

In this work, the main goal was to shed light on the impact of Brønsted/Lewis acidity modulation of Pt-supported catalysts in the acetone HDO reaction, a representative molecule for ketone-containing oxygenates derived from biomass. Acidity modulation was achieved using Ti-Nb mixed oxide supports with different Nb at% loadings. The nanotubular morphology was chosen since it favors high specific surface areas (SSA) and more defective and disordered structures [29–31]. Detailed studies at the atomic scale of these materials were conducted and were crucial for understanding some fundamental aspects related to structural and electronic properties, active sites, and reaction mechanisms. Moreover, we highlight essential insights into the connection between MSI and acid sites for Pt-supported over metal oxides and discuss some fundamental correlations between catalytic sites and reaction mechanisms for the acetone HDO reaction.

2. Experimental section

Complementary detailed information about the materials and catalyst characterization was included as Supporting Information (**Experimental Section**).

2.1. Metal oxide supports' synthesis

Ti-Nb metal oxide supports were synthesized using a hydrothermal method, similar to previously reported works [16,21,22]. Before the synthesis, the Nb$_2$O$_5$ precursor was dried in a vacuum oven for 1 h and sifted in an 80-mesh sieve. It was dispersed in 50 mL of a 10 mol L^{-1}

NaOH solution by stirring for 10 min and sonicating it for 20 min. TiO$_2$ precursor was added to the mixture and stirred for 10 min, sonicated for 30 min, stirred for 3 h, and finally sonicated for 20 min. For the synthesis of pure TiO$_2$, only the last procedure steps were conducted. The mixture was kept in a Teflon-lined stainless-steel autoclave at 200 °C for 6 h. The solid was washed with 0.1 mol L^{-1} HCl solution up to pH 3 and was kept under stirring for 1 h; it was filtered and washed with distilled water until complete NaCl removal (verified with AgNO$_3$ solution). Finally, it was oven dried at 100 °C and calcined at 400 °C for 1 h, with a heating rate of 5 °C min^{-1}. The metal oxide supports were labeled according to the Nb at% loading, i.e., 0 (for pure TiO$_2$), 2.5, 5, 10, 25, 50, and 100 at % Nb. The syntheses were conducted using a total mass of 750 mg of the precursors and different Ti: Nb at% proportions.

2.2. Catalyst preparation

Pt-supported catalysts (1 wt%) were obtained through a wet impregnation method. Before the impregnation, 8.6 mg of K$_2$PtCl$_4$ was dispersed in 2 mL of DMSO for ligand exchange and rested overnight. 400 mg of the metal oxide support was dispersed in 100 mL of ethanol and sonicated for 1 h. Pt precursor solution was added to the mixture under stirring, drop by drop, and sonicated for 1 more hour. The sonicator bath was heated up to 50 °C, and the mixture was sonicated until total evaporation of the solvent. The solid was oven dried at 80 °C overnight and calcined at 400 °C for 1 h, with a heating rate of 5 °C min^{-1}. The Pt-supported catalysts were labeled according to the support, i.e., 0 at% Nb 1 wt% Pt and 25 at% Nb 1 wt% Pt.

2.3. Catalytic evaluation

Acetone hydrodeoxygenation (HDO) reaction was conducted in a plug-flow tubular reactor equipped with a quartz tube (inner diameter of 8.1 mm), with a catalytic bed composed of 50 mg of catalyst and 150 mg of diluent (quartz powder; <100 mesh). Acetone was introduced into the reactor by a saturator flask (3.6 mL min^{-1} of acetone) using He as carrier gas. H$_2$ was also fed to the reactor (76 mL min^{-1}; 21 mol H$_2$:mol acetone), with a total feed flow of 100 mL min^{-1}, with He for balance. All flows were measured at the ambient temperature of 25 °C. These reaction parameters were optimized in a previous work [32]. The catalytic tests were performed as a function of temperature (100–400 °C, with 100 °C steps, 30 min at each temperature) or as a function of time on stream (TOS), at 400 °C for 6 or 20 h. For the metal-supported catalysts, a reduction step was conducted at 400 °C for 1 h before the reaction, with 10% H$_2$ in He, with a total flow of 100 mL min^{-1}. The products were analyzed by an online gas chromatograph (GC; Agilent Technologies, model 7890 A) equipped with an HP-1 column (50 m x 0.32 mm i.d., 0.17 μm).

Acetone conversion (Eq. 1), products distribution (Eq. 2), selectivity (C-mol basis, Eq. 3), degree of deoxygenation (DOD, Eq. 4), and carbon balance (Eq. 5) were calculated as follows:

$$Conversion \quad (\%) = \frac{moles_{acetone \ \ in} - moles_{acetone \ \ out}}{moles_{acetone \ \ in}}.100 \tag{1}$$

$$Products \quad distribution = \frac{moles \ \ of \ \ product \ \ i}{moles \ \ of \ \ total \ \ products} \tag{2}$$

$$Selectivity \ (C - mol) = \frac{Carbon \ moles \ of \ product \ i}{Carbon \ moles \ of \ acetone \ consumed} \tag{3}$$

$$Degree \ of \ deoxygenation \ (DOD) = \frac{moles \ of \ deoxygenated \ products}{moles \ of \ total \ products} \tag{4}$$

$$Carbon \quad balance = \frac{moles \ \ of \ \ C \ \ of \ \ total \ \ products}{moles \ \ of \ \ C \ \ of \ \ acetone \ \ fed} \tag{5}$$

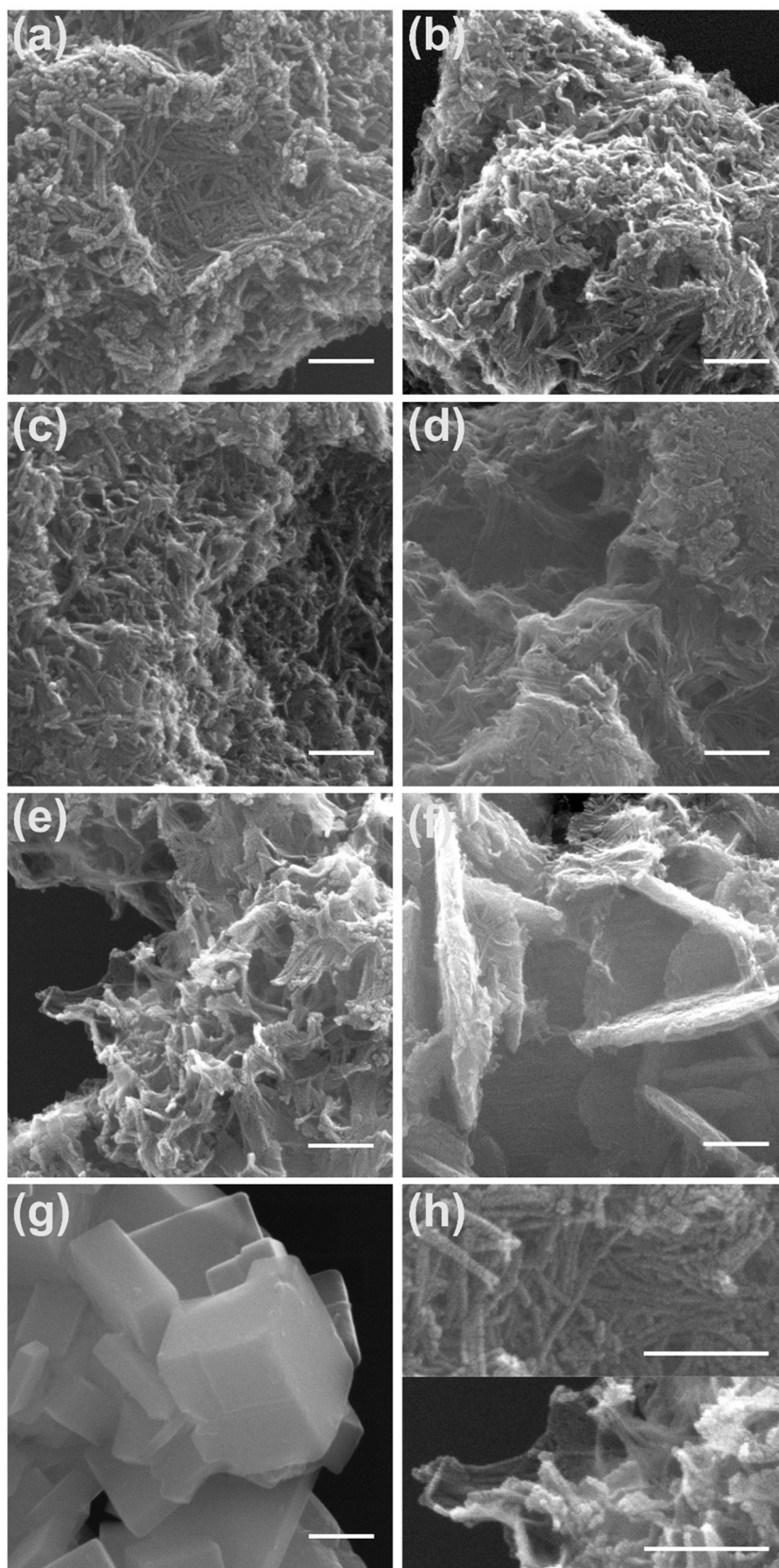The main products detected in acetone HDO were CH$_4$, propylene/

Fig. 1. SEM micrographs of the synthesized metal oxides: (a) 0 at% Nb, (b) 2.5 at% Nb, (c) 5 at% Nb, (d) 10 at% Nb, (e) 25 at% Nb, (f) 50 at%, and (g) 100 at% Nb. In (h), zoomed in regions of (a, top) and (e, bottom), highlighting the nanotubular morphology. Scale bar of 200 nm.
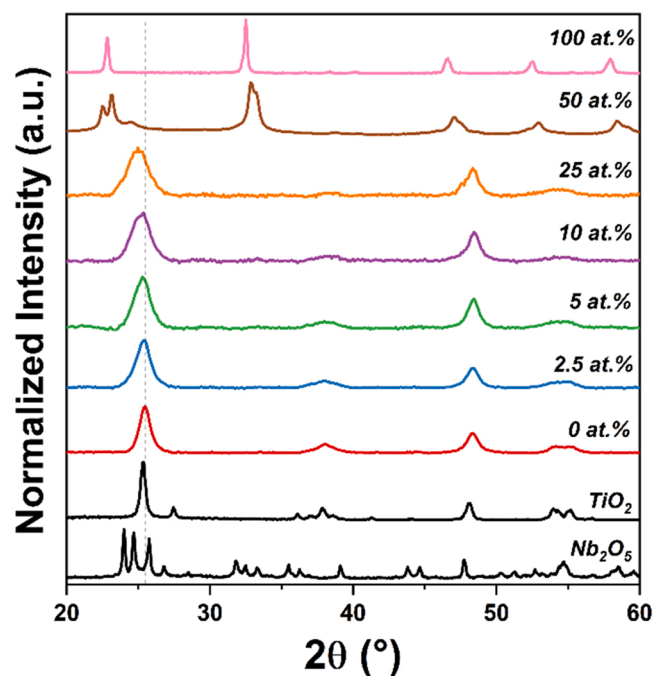
Fig. 2. Normalized XRD patterns of TiO_2 and Nb_2O_5 precursors and the synthesized metal oxides using different Nb at% loadings.
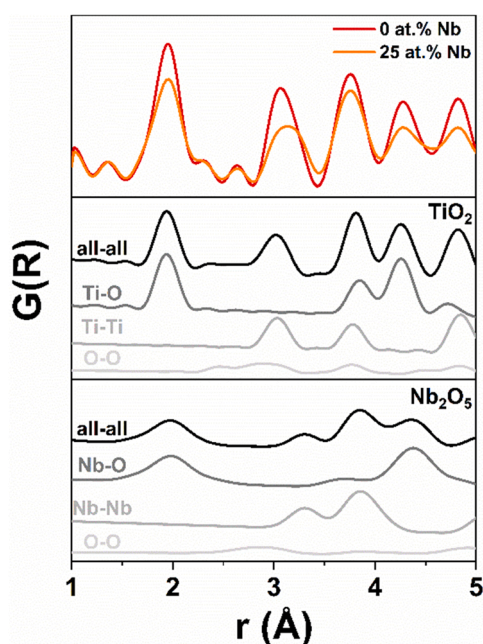

Fig. 3. (Top) Experimental PDF profiles of 0 and 25 at% Nb supports and TiO_2 anatase (middle) and Nb_2O_5 (bottom) deconvoluted patterns for comparison. Each atomic pair contribution is presented, and all-all represents the sum of all contributions.

propane (C_3), isobutene/isobutane (C_4), 2-methyl-pentene/2-methyl-pentane (C_6), isopropanol (IPA), 4-methylpent-3-an-2-one/4-methyl-pentan-2-one (C_6O), and 2,6-dimethyl-4-heptanone and its position isomers (C_9O). The molar sum of the deoxygenated products CH_4, C_3, C_4, and C_6 was used for the DOD calculation.

3. Results and discussion

In the hydrothermal synthesis, the strongly basic conditions, pressure, and temperature led to the dissolution of the precursors (TiO_2 and Nb_2O_5) and recrystallization forming the mixed oxides. SEM micrographs of the synthesized materials (Fig. 1) demonstrated that nanotubular morphology was obtained for 0 at% Nb sample (pure TiO_2), while partial nanotube formation seemed to occur along the Nb content increase up to 25 at% Nb. The substitution of Ti sites by Nb hindered part of the structure from curling, forming some sheet-like morphology structures along with nanotubes, consistent with previous reports on similar materials [16,33]. These morphological modifications were confirmed by the TEM analysis. Figs. S2 and S3 display representative images of the 0 at% Nb and 25 at% Nb samples, respectively. More expressive morphological modifications were observed for Nb contents ≥ 50 at% (Fig. 1), which were consistent with perovskite structure formation.

Fig. 2 shows the XRD data of the synthesized metal oxides in comparison with the TiO_2 and Nb_2O_5 precursors. The 0 at% Nb pattern corresponds to the anatase crystal structure (ICSD CollCode121633), in which the low intensity and broadening of the diffraction peaks indicate the formation of nanosized crystalline domains. Although the Nb addition impacted the morphology of the materials (Fig. 1), XRD data indicate that Nb atoms were incorporated into TiO_2 anatase crystal structure up to Nb contents of 25 at%. Slight shifts to lower 2-theta angles and broadening of the (101) peak were observed along with Nb content increase (Fig. S4), indicating an expansion (up to 18%) of the unit cell along the c-axis (no significant variations were observed for the a-axis) and the formation of smaller crystallite sizes (5–10 nm range), respectively (Table S1). When the Nb content was 50 at%, the XRD resembles the mixed $NaNb_{1-x}Ti_xO_{3-0.5x}$ perovskites [34], but the asymmetrical and doublet peaks indicate more pronounced and inhomogeneous distortions of the crystal lattice and/or the coexistence of different crystalline phases/polymorphs. For Nb at. content of 100%, a pure phase of $NaNbO_3$ (ICSD CollCode142291) was observed. It is also important to note that diffraction peaks related to Nb_2O_5 crystal phases were not identified in the XRD patterns.

The low intensity and the broadening of the diffraction peaks up to 25 at% Nb point to structures with short- and medium-range order that cannot be accessed by analyzing the Bragg peaks. Then, the total scattering and PDF analysis were performed, and the PDF profile was obtained through the Fourier transform of the total scattering pattern, experimentally obtained by measuring the scattering patterns with a high magnitude of the scattering vector (Q, usually above 25 $Å^{-1}$) [34]. PDF analysis provides data in the real space, which can be related to the Bragg scattering and to short and medium-range order information from the diffuse scattering intensity of the sample, e.g., disordered and nanostructured materials [34].

Short-range PDF profiles (≤ 5 Å) of 0 at% Nb and 25 at% Nb samples are presented in Fig. 3, together with PDF profiles of TiO_2 (anatase) and Nb_2O_5 (ICSD CollCode17027), both with tetragonal phases. Medium-range PDF profiles (≤ 50 Å) are shown in Fig. S5. As depicted in Fig. 3, each pattern presents different pair contributions, which can be associated with the peaks observed for the synthesized metal oxides. It is possible to observe that the insertion of 25 at% Nb into the TiO_2 structure led to a clear dampening of the peaks above ~ 30–40 Å (Fig. S5), indicating smaller crystallite sizes, corroborating the XRD data analysis (Fig. 2, S4, and Table S1). Moreover, a broadening of the PDF peaks was also observed, which can be related to a more distorted and defective structure [35,36]. The first peak (1.95 Å) is assigned to Ti-O and/or Nb-O first shell pairs, in which the insertion of Nb led to a broader and less intense peak, suggesting the formation of oxygen vacancies [37–39]. The peak at 3.08 Å is associated with Ti-Ti, Ti-Nb, and Nb-Nb pairs, and it is clear that Nb addition led to a more pronounced atomic displacement of these pairs. Overlapping of the PDF peaks occurred at higher interatomic distances, encompassing metal-metal, metal-oxygen, and

Table 1
Nominal and surface Nb at% loadings and their ratios, O/(Ti+Nb) ratios, and specific surface areas of the mixed oxides.

Sample	Nominal Nb loading (at%)[a]	Surface Nb loading (at%)[a,b]	Ratio between surface/ nominal Nb loading	O/ (Ti+Nb)[b]	Specific Surface Area (m^2 g^{-1})[c]
0 at% Nb	0	0	-	2.3	238
2.5 at% Nb	2.5	6.6	2.6	2.2	348
5 at% Nb	5	10.8	2.1	2.0	306
10 at% Nb	10	13.7	1.4	2.0	331
25 at% Nb	25	27.6	1.1	1.8	290
50 at% Nb	50	56.9	1.1	1.4	108
100 at% Nb	100	100	1	2.7	17

[a] 100 *Nb/(Nb+Ti), [b] obtained through XPS data; [c] determined by N_2 physisorption measurements

oxygen-oxygen pairs (Fig. 3). Despite the differences, the overall profile of the TiO$_2$ anatase was preserved in 25 at% Nb, in agreement with the incorporation of the Nb atoms into the TiO$_2$ lattice.

XPS spectra of the Ti 2p region (Fig. S6a) show the Ti 2p$_{3/2}$ and 2p$_{1/2}$ peaks around 458.7 eV and 464.5 eV, respectively, with a doublet splitting of 5.7 eV, in agreement with the presence of Ti^{4+} species [40, 41]. XPS spectra of the Nb 3d region are presented in Fig. S6b. Nb 3d$_{5/2}$ and 3d$_{3/2}$ peaks of the Nb$_2$O$_5$ precursor were observed at 207.6 eV and 210.3 eV, respectively, with a doublet splitting of 2.7 eV [41]. The XPS spectra of the synthesized oxides presented shifts to lower BE compared to the Nb$_2$O$_5$ precursor, suggesting changes in the chemical environment around Nb species [42]. By comparing the synthesized oxides with Nb contents up to 25 at%, it was possible to notice that the BE of the Nb 3d$_{5/2}$ and 3d$_{3/2}$ contributions did not change, with peaks at 207.1 eV and 209.9 eV, respectively. This suggests that Nb species and their chemical environment were similar, corroborating Nb incorporation into TiO$_2$ anatase crystal structure. However, a different behavior was observed when perovskite crystal structure was formed ($\geq$ 50 at% Nb), shifting to lower BE. In particular, the BE of Nb 3d$_{5/2}$ and 3d$_{3/2}$ peaks from the 100 at% Nb sample, i.e., NaNbO$_3$ crystal structure, is compatible with previous reports, appearing at 206.5 eV and 209.3 eV, respectively [43].

Total elemental surface quantification through XPS measurements (Table S2) demonstrated that the synthesis procedure led to residual Na in the samples' surface, while no residual Cl was observed. For the materials with Nb at. contents up to 25% the Na content was similar (3.3–3.8 at%) and did not impact the crystal structures (Fig. 2 and 3). Elemental surface quantification of Nb (Nb/(Nb+Ti) ratio) was also obtained through XPS data, as presented in Table 1. The ratio between surface and nominal Nb content demonstrated that there was an enrichment of Nb on the surface of the oxides for lower loadings. However, this ratio decreased with the increase of Nb at% content, up to ratios of 1.1, close to their nominal values. The surface ratio between oxygen and metals (Nb + Ti) was also calculated (Table 1). For the synthesized oxides up to 25 at% Nb, where Nb was inserted into TiO$_2$ anatase crystal structure, it was possible to observe that this ratio decreased with Nb content increase. This could be associated with the formation of oxygen vacancies due to Nb substitution over Ti sites, in agreement with PDF data (Fig. 3). Similar results in Ce-Nb mixed metal oxides were also obtained [39]. Nb 3d peak shifts to lower BE also suggest more reduced Nb species than that observed for the Nb$_2$O$_5$ precursor (Fig. S6b), corroborating this hypothesis.

The SSA of the synthesized oxides was also affected by Nb addition. SSA of 238 m^2 g^{-1} was obtained for the 0 at% Nb sample, while the addition of Nb up to 25 at% led to SSAs varying from 290 to 348 m^2 g^{-1} (see Table 1). A decrease in the SSA was observed for the samples of 50 and 100 at% Nb, to 108 and 17 m^2 g^{-1}, respectively, associated with the perovskite structure formation. The data presented so far corroborate that Nb was successfully inserted into TiO$_2$ anatase crystal structure up to 25 at% Nb; thus, further discussion will be focused on these samples.

Spectroscopic techniques invoking the adsorption of probe molecules have been extensively employed in determining the nature, strength, and concentration of acid sites in solid catalysts [44]. FTIR-monitored

Py adsorption has the advantage of detecting Brønsted and Lewis acid sites simultaneously. As shown in the spectra (Fig. 4a), the bands at ~1546 and ~1446 cm^{-1} can be attributed to Py adsorbed at Brønsted and Lewis acid sites, respectively, whereas the additional band at ~1490 cm^{-1} has contributions from both sites [45,46]. It is possible to visualize an increase in Brønsted/Lewis (B/L) ratio alongside the Nb content in the catalysts (Fig. 4c and Table 2), demonstrating that Nb insertion into TiO$_2$ structure leads to materials richer in Brønsted acid sites. The genesis of these sites can be associated with H$_2$O coordination to highly polarized Nb–O as a result of distortions in the NbO$_6$ octahedra [47–49]. PDF data (Fig. 3) indicated that a more distorted structure was obtained upon Nb addition, corroborating the Brønsted acidity increase.

A quantitative approach was also performed through TMPO adsorption experiments monitored by ^{31}P NMR analysis. The use of phosphine oxides for this purpose has shown to be reliable and sensitive, especially in probing Brønsted acid sites [50,51]. The ^{31}P nuclei have 100% isotopic abundance and offer high-resolution NMR signals due to a combination of a ½-spin, a sufficiently high gyromagnetic ratio, and a wide range of chemical shifts [52]. Additionally, there is a linear correlation between the chemical shift of adsorbed TMPO and the deprotonation energy of the TMPOH$^+$-complexed species when anchored to Brønsted acid sites of various acid strengths [52]. In this case, the spectra commonly present a broad and overlapping distribution of resonances, in which higher chemical shifts are assigned to sites where TMPO is more strongly adsorbed [52]. The ^{31}P NMR spectra (Fig. 4b) show single broad signals in ~50 to ~80 ppm, characteristic of metal oxides [53–55]. Different contributions were obtained from the deconvolution of the signals [56], where four contributions were attributed to Brønsted acid sites with different strengths (B1-B4) and one to Lewis acid sites (L), evidencing the fact that TMPO is more sensitive to Brønsted acid sites. For this reason, the B/L ratios obtained by ^{31}P NMR were higher than the ones obtained by Py-FTIR for the same Nb at% loadings; however, the same tendency could be verified through both techniques (Fig. 4c).

The total acidity of the catalysts was estimated by P elemental analysis of the TMPO-loaded samples through the direct correlation between the number of P atoms and acid sites. It was possible to verify that the insertion of Nb into the TiO$_2$ structure increased the total acidity (Table 2). The 0 at% Nb sample presented 381 μmol g^{-1} of acid sites, while the samples from 2.5 to 25 at% Nb presented between 462 and 602 μmol g^{-1}. Although there is no linear correlation between the Nb loading and the total acid site concentration, there was a significant increase upon the addition of Nb compared to the pure TiO$_2$ sample. Considering that the SSAs of the mixed oxides varied depending on the Nb at% loading (Table 1), the acid sites distribution per accessible area was determined (Table 2), demonstrating that all samples present similar values, between 0.84 and 1.18 sites per nm^2. Additionally, the total acidity and acid sites per area were determined for each contribution observed in the ^{31}P NMR spectra (Fig. 4b and Tables S3-S4).

Based on the characterization of the acidic properties of these materials, it was possible to demonstrate that the formation of the mixed oxides led to Brønsted and Lewis acidity modulation. The B/L acid sites ratio increased along with the Nb content, showing that Nb insertion into the TiO$_2$ lattice led to mixed oxides richer in Brønsted acid sites but
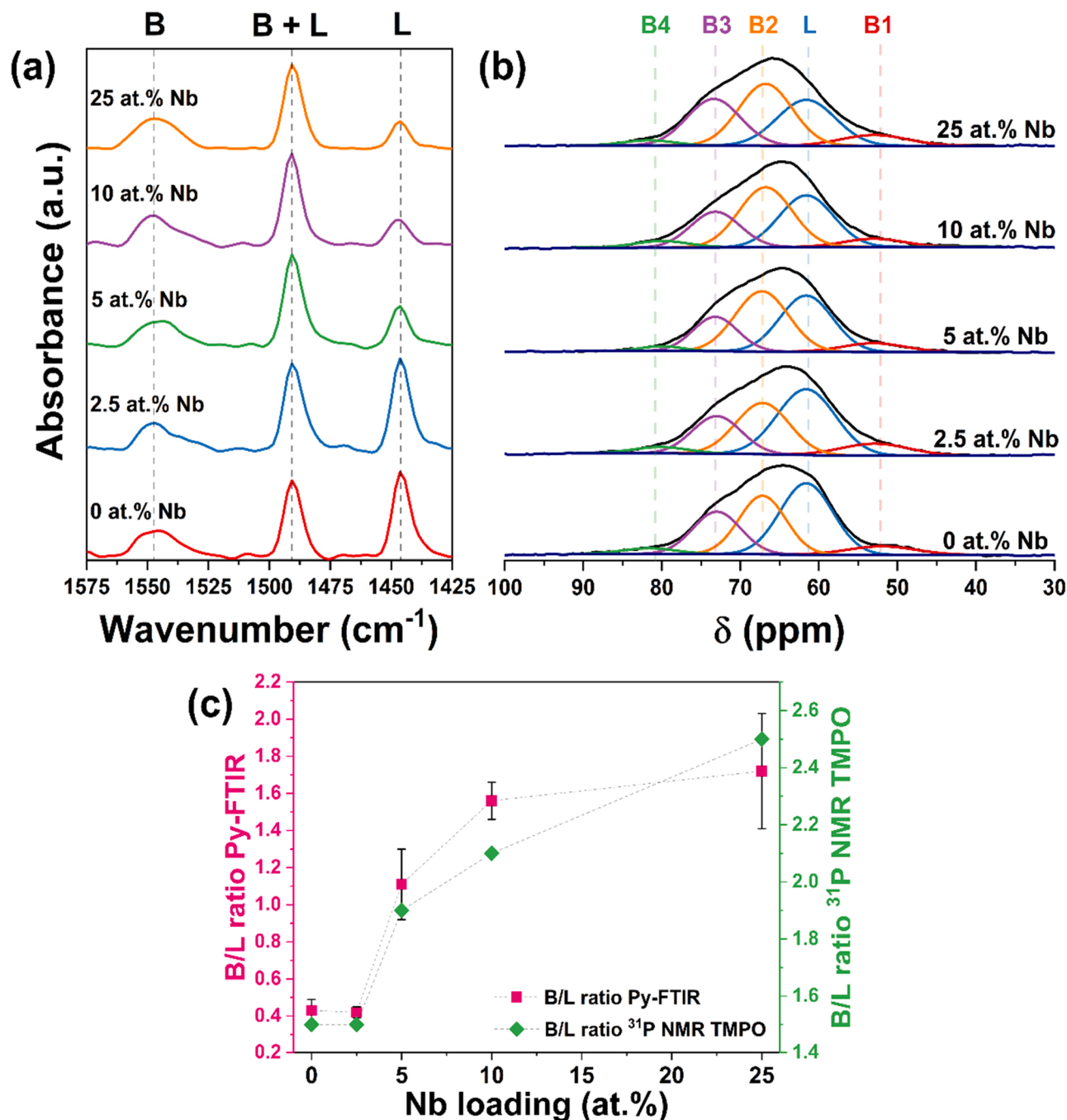
Fig. 4. Acid site characterization of mixed metal oxides up to 25 at% Nb using (a) Py-FTIR and (b) ^{31}P NMR of TMPO at 240 MHz; (c) Brønsted/Lewis acid sites ratio dependence on Nb at% loading. B stands for Brønsted acid sites, and L for Lewis acid sites. B1 to B4 stands for Brønsted acid sites with different strengths, in which the higher the number, the stronger the site.

keeping similar values of the overall acid sites per area.

To evaluate the impact of the acidity modulation of the Ti-Nb mixed metal oxides in the acetone HDO reaction, 1 wt% Pt (a hydrogenating metal) was impregnated over 0 at% Nb and 25 at% Nb supports. These supports were characterized by anatase crystal structure, and similar morphologies and SSAs. Scheme 1 presents in more detail the acetone HDO reaction network proposed for the catalysts employed in this work, encompassing metallic sites (MS), Brønsted/Lewis acid sites (AS), and oxygen vacancy sites (OVS) that can catalyze different pathways. Starting from acetone, three main parallel pathways have been proposed: hydrogenation leading to IPA; hydrogenation/dehydration leading to C_3, and condensation intermediary steps leading to C_6O, C_9O,

C_4, CH_4, and C_6 [4,32].

The catalysts were evaluated in temperatures ranging from 100° to 400°C. Both catalysts showed activity and hydrogenation capability at temperatures ≤ 200 °C, where IPA was the main product (Fig. 5a). At temperatures above 300 °C, acetone conversions and DODs significantly increased, showing conversions higher than 70% (>135 $mmol_{acetone}$ g_{cat}^{-1} h^{-1}) and DODs above 90%. At 400 °C, conversions and DODs were both greater than 90% (>174 $mmol_{acetone}$ g_{cat}^{-1} h^{-1}), with C_3 and C_6 as the main products. However, no significant variations in the conversion and products distribution were observed between the catalysts, suggesting that the acidity modulation introduced by the Nb did not impact, to a great extent, the catalytic results at shorter TOS. Additionally, both

Table 2
Brønsted/Lewis (B/L) acid sites ratio determined by Py-FTIR and ^{31}P NMR of adsorbed TMPO, total acidity, and acid sites per area of the mixed metal oxides. B stands for the sum of all Brønsted acid sites.

Sample	B/L acid sites ratio Py-FTIR[a]	B/L acid sites ratio ^{31}P NMR[b]	Total acidity (μmol g^{-1})[c]	Acid sites per area (sites nm^{-2} x 10^{-2})
0 at% Nb	0.43 ± 0.06	1.5	381 ± 21	96 ± 5
2.5 at% Nb	0.42 ± 0.03	1.5	522 ± 29	90 ± 5
5 at% Nb	1.1 ± 0.2	1.9	602 ± 5	118 ± 1
10 at% Nb	1.5 ± 0.1	2.1	462 ± 8	84 ± 1
25 at% Nb	1.7 ± 0.3	2.5	527 ± 22	109 ± 5

[a] determined by Py-FTIR; [b] determined by ^{31}P NMR of adsorbed TMPO; [c] determined by ICP-OES of P.

Lewis and Brønsted acid sites can mediate dehydration reactions at high temperatures ($\geq 350\,°C$) [57], which could explain the similarity between the catalytic performances. For comparison, the bare 0 at% Nb and 25 at% Nb supports were also evaluated; both were active in the acetone HDO but favored condensation products at lower temperatures ($\leq 200\,°C$) and some deoxygenation at 400 °C (Fig. 5b). The acetone conversions were ~50% (~100 mmol$_{acetone}$ g$_{cat}^{-1}$ h^{-1}) at 400 °C, with DODs varying from 28% to 35%. Condensation products formation was still high (~65%) for both supports at 400 °C, demonstrating the prevalence of the acid sites and their important role in C–C coupling reactions in the absence of Pt. No significant changes in the products distribution were also observed between the bare 0 at% Nb and 25 at% Nb supports (Fig. 5b) and the other mixed oxides with lower Nb at% contents (Fig. S7).

Stability tests were conducted to identify whether the acidity modulation could impact the performance of these catalysts under longer TOS. The tests were conducted at 400 °C for both sets, the Pt-supported catalysts and the bare supports. Concerning the bare mixed oxides, both 0 at% Nb (Fig. 6a) and 25 at% Nb (Fig. 6b) presented similar catalytic performances, with conversions around 40% (~77 mmol$_{acetone}$ g$_{cat}^{-1}$ h^{-1}), favoring condensation products formation along the TOS, mainly C$_6$O. The condensation products originate from C–C coupling reactions over the acid sites, while C$_4$ formation is associated with the β-scission of condensation products, i.e., C$_6$O and C$_9$O, over Lewis and Brønsted acid sites [58,59]. The DODs of both supports also presented a fast decrease during the first hour on stream (Fig. 6e), and the deactivation rate (9.5×10^{-4} h^{-1}) was the same for both (Fig. 6f).

On the other hand, the evolution of products distribution with TOS was significantly different for the Pt-supported catalysts (Fig. 6c,d). By employing the 0 at% Nb 1 wt% Pt catalyst (Fig. 6c), the initial 3 h on stream favored the formation of propane and C$_6$ products, with conversions higher than 60% (>116 mmol$_{acetone}$ g$_{cat}^{-1}$ h^{-1}). These two products can be formed through a bifunctional mechanism associating metallic and acid sites, Scheme 1 [32]. However, after 3 h on stream, the

formation of condensation products and propene became favored, demonstrating that the hydrogenation capability of the catalyst was affected. After 20 h on stream, C$_6$O represented 72.6% of the products distribution, suggesting a deactivation of the MS and the prevalence of AS from the support.

The initial hours on stream for the 25 at% Nb 1 wt% Pt catalyst (Fig. 6d) was similar to that observed for the 0 at% Nb 1 wt% Pt one, where propane and C$_6$ products were favored. In this case, however, changes in the products distribution were slower over TOS. At 8 h on stream, propene and propane products distribution were almost the same and together represented about 60% of the obtained products. Propene was steadily formed up to 20 h on stream. After 20 h on stream, propene was the main product, representing 29.3% of the total products, followed by C$_6$O (28.3%), C$_9$O (16.7%), propane (14.9%), and the other products (10.8%).

While the DOD significantly decreased for 0 at% Nb 1 wt% Pt catalyst, down to 17.2% after 20 h on stream, the 25 at% Nb 1 wt% Pt catalyst led to a DOD more than 3 times higher (Fig. 6e). Since the DOD was primarily associated with the presence of MS, it can be inferred that the MS were much more stable in the presence of Nb.

Further catalytic tests were done to better understand the deactivation mechanisms. As presented in Fig. 6f, two main deactivation steps took place along the TOS for both Pt-supported catalysts: the first one associated with a fast deactivation and concomitant loss in deoxygenation capability (Fig. 6e), and the second one characterized by a lower deactivation rate. Deactivation can be generally attributed to the deposition of coke on the catalyst surface, poisoning due to the adsorption of intermediate species in the active sites during the reaction, or sintering of metallic particles [60,61]. The change in selectivity and the decrease of the DOD along TOS indicate the presence of different catalytic sites that deactivate at different rates.

The regeneration of the 0 at% Nb 1 wt% Pt catalyst was conducted under an oxidizing atmosphere. It was possible to successfully recover the performance of the fresh catalyst (Fig. S8), indicating that the main
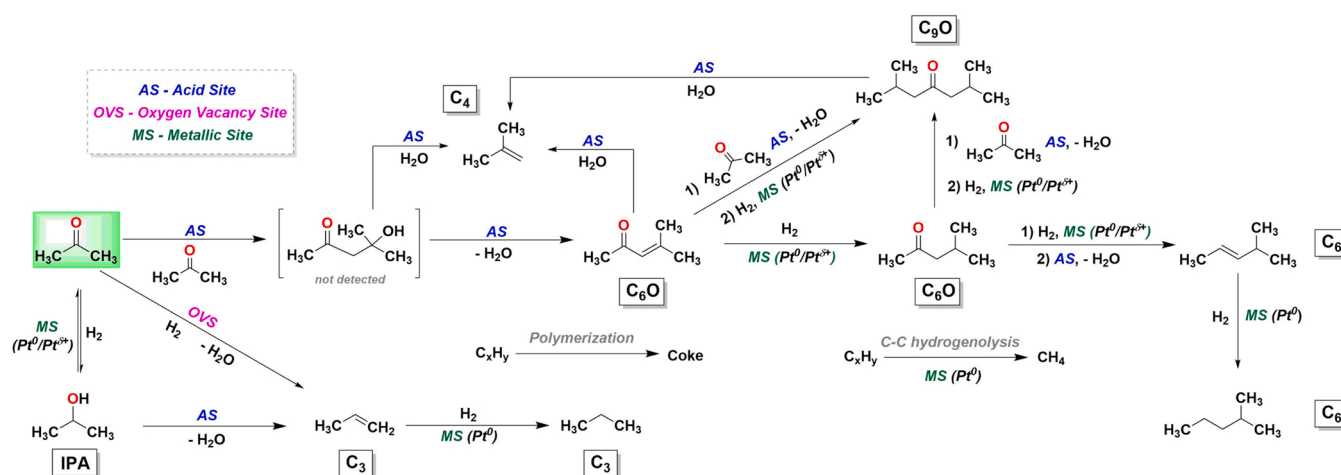
Scheme 1. Proposed acetone HDO reaction network for Pt-supported Ti-Nb mixed metal oxide catalysts employed in this work.
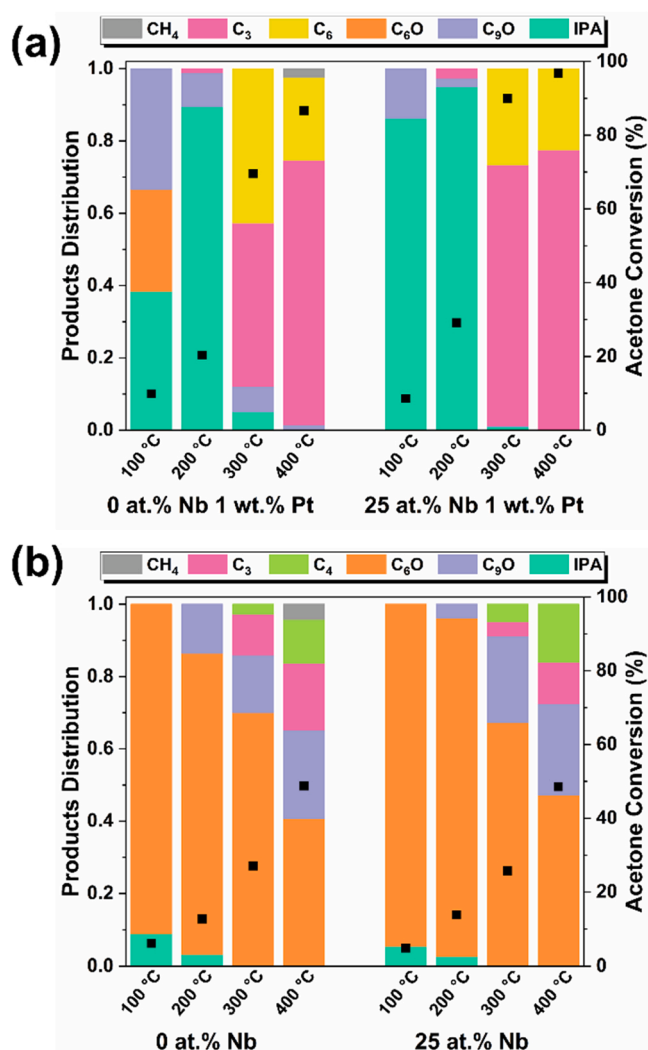
Fig. 5. Products distribution (bars) and conversion (squares) of acetone HDO reaction as a function of temperature (100–400 °C) for (a) 0 at% Nb 1 wt% Pt and 25 at% Nb 1 wt% Pt; and (b) 0 at% Nb and 25 at% Nb (bare supports). Total feed of 100 mL min^{-1}: 3.6 mL min^{-1} acetone, 76 mL min^{-1} H$_2$, balance He. Catalyst mass: 50 mg. Soaking time at each temperature of 30 min.

deactivation occurred due to coke formation. The carbon balance over TOS (Fig. S9), and Raman spectrum and TG analysis of the post-reaction catalyst (Figs. S10 and S11), complemented by the similar performance obtained after regeneration of the catalyst under an oxidizing atmosphere (Fig. S8) corroborate that the main deactivation occurred due to coke formation. The same catalyst was also submitted to a reducing thermal treatment (using H$_2$) to evaluate whether poisoning by chemisorbed molecules could contribute to the deactivation, but this treatment did not have any effect (Fig. S12). Finally, to assess if the harsh reducing environment of the reaction could lead to Pt particles sintering and/or encapsulation by TiO$_x$ species due to the well-known SMSI effect between Pt-supported over TiO$_2$ [11], a pretreatment under 70% H$_2$ was conducted at 400 °C for 6 h before reaction. In this case, no significant variations were observed compared to that pretreated under 10% H$_2$ at 400 °C for 1 h (Fig. S13). Together, the analysis of the catalytic performance of the 25 at% Nb 1 wt% Pt catalyst after regeneration under oxidizing atmosphere (Fig. S14), the carbon balance over TOS (Fig. S9), and the results obtained by analyzing the post-reaction catalyst by Raman spectroscopy and TG analysis (Figs. S10 and S11) corroborate that the main deactivation also occurred due to coke formation. Although the 25 at% Nb 1 wt% Pt catalyst presented a higher DOD over

TOS, coke deposition was more extensive, representing about 7.6 wt%, against 4.6 wt% for the 0 at% Nb 1 wt% Pt one. Moreover, Raman spectra of both post-reaction catalysts (Fig. S10) demonstrated that the carbonaceous species did not significantly differ, presenting similar D-/G-band ratios (0.41–0.45). Whereas the D-band characterizes a more defective and disordered carbonaceous structure that rises from out-of-plane vibration, the G-band characterizes a more graphitic structure, originated from in-plane vibrations of C-C bonds. The ratio found for both catalysts indicates that a highly disordered graphitic structure was accumulated on their surface, in which the genesis of the disorder could be either morphologically and/or structurally related.

To further evaluate the effect of coke deposition on the catalytic performance, the selectivity of the catalysts over TOS was also presented taking into account coke as a product, on a C-mol basis distribution (Fig. S15). It is possible to notice that both supports (Figs. S15a,b) presented coke selectivities of about 30–40%, which were steadily maintained up to 6 h on stream. For 0 at% Nb 1 wt% Pt, coke selectivity increased at the initial 4 h on stream, up to about 50%; at the same time, propane and C$_6$ selectivities quickly decreased, demonstrating that the deactivation of the MS was concomitant with coke deposition. After 4 h on stream, coke selectivity decreased along with C$_6$O selectivity increase. While for 25 at% Nb 1 wt% Pt, coke selectivity increased up to about 45% after 6 h on stream, with a concomitant drop in the hydrogenation capability, as observed through the decrease in propane and C$_6$ selectivities. After 8 h on stream, coke selectivity was kept steady and the hydrogenation capability was more stable, gradually dropping over TOS. Nevertheless, the total selectivity to deoxygenated products for the 25 at% Nb 1 wt% Pt catalyst was 2.5-fold greater than for 0 at% Nb 1 wt % Pt after 20 h on stream.

TEM analysis was conducted over the reduced catalysts to get insight into the Pt dispersion. A major population (about 95%) of Pt nanoparticles with a mean diameter of 4.4 ± 2.6 nm was observed for the reduced 0 at% Nb 1 wt% Pt catalyst (Fig. 7a,b). A minor population of larger particles was also present, with a mean diameter of 26.3 ± 7.3 nm. Smaller particles were observed for the reduced 25 at% Nb 1 wt% Pt catalyst, as presented in Fig. 7c-d (red dashed circles and arrows highlight some of the particles in Fig. 7c), with a mean diameter of 2.5 ± 1.5 nm. For better visualization of the predominance of these small Pt particles in the 25 at% Nb 1 wt% Pt catalyst, a HAADF-STEM image is presented in Fig. S16. XRD measurements (Fig. S17) corroborated the TEM analysis; the Pt (111) main peak was only detected in the XRD pattern of the 0 at% Nb 1 wt% Pt catalyst due to the presence of larger particles (mean crystallite size of 9 nm). The HR-TEM images of representative Pt particles showed the interplanar spacing of 0.22 nm (Fig. 7b,d), corresponding to the (111) lattice planes of metallic Pt species with cubic crystal structure (ICSD CollCode243678). Histograms of the particle size distribution of both Pt-supported catalysts are presented in Fig. S18. Since the SSA of the bare supports were similar (Table 1), the better dispersion of the metallic phase on the 25 at% Nb 1 wt% Pt catalyst can be associated with a stronger MSI due to the presence of Nb.

XPS measurements of calcined, reduced (pre-reaction), and post-reaction Pt-supported catalysts are presented in Fig. 8. XPS measurements fitting parameters for Pt 4f region are presented in Table S5. Both calcined catalysts presented similar Pt/(Ti+Nb) ratios (Table S6), demonstrating that their dispersions were quite similar before reduction. However, the ratios between Pt/(Ti+Nb) of reduced and post-reaction catalysts were affected by the presence of Nb; it decreased in the 0 at% Nb 1 wt% Pt catalyst while it was not significantly affected in the 25 at% Nb 1 wt% Pt catalyst, in agreement with TEM (Fig. 7 and S16), and XRD data (Fig. S17). Pt species also varied for the calcined catalysts: both Pt^{2+} and metallic (Pt^0) species were observed in 0 at% Nb 1 wt% Pt catalyst, whereas in the 25 at% Nb 1 wt% Pt catalyst only Pt^{2+} species were observed (Pt^0 can be formed together with O$_2$ through PtO decomposition during calcination of Pt/TiO$_2$ systems conducted at ≥ 400 °C [62,63]). On the other hand, both reduced catalysts presented
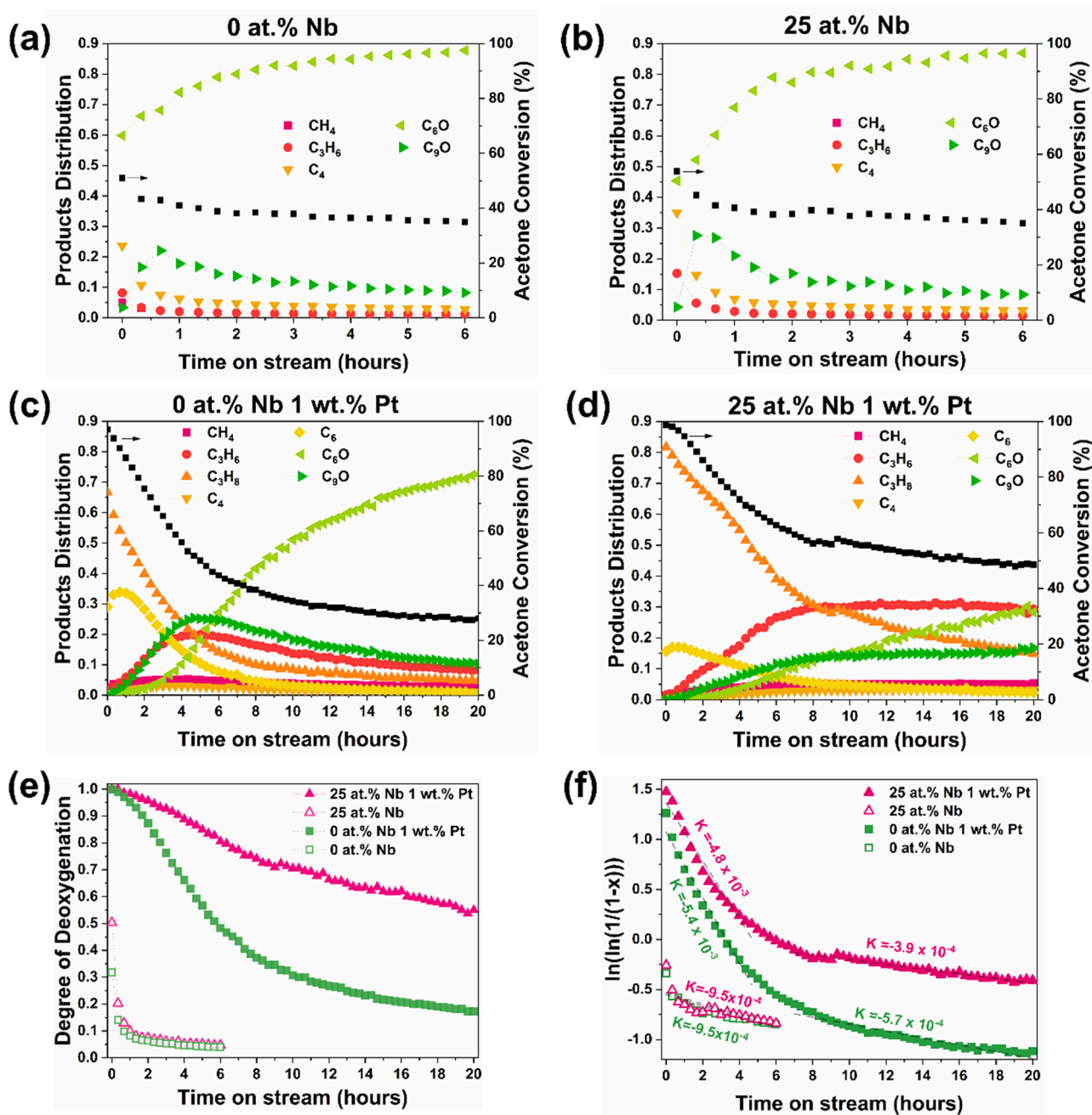
Fig. 6. Conversion (black squares) and products distribution of acetone HDO reaction at 400 °C as a function of TOS for (a) 0 at% Nb, (b) 25 at% Nb, (c) 0 at% Nb 1 wt% Pt, and (d) 25 at% Nb 1 wt% Pt; (e) Degree of deoxygenation and (f) deactivation rates of the catalysts over TOS. Total feed of 100 mL min^{-1}: 3.6 mL min^{-1} acetone, 76 mL min^{-1} H$_2$, balance He. 50 mg of catalyst for each test.

partially oxidized (Pt$^{\delta+}$) and Pt^0 species; the 0 at% Nb 1 wt% Pt catalyst was richer in metallic species (Pt$^{\delta+}$/Pt^0 ratio of 0.6), while the 25 at% Nb 1 wt% Pt was richer in Pt$^{\delta+}$ species (Pt$^{\delta+}$/Pt^0 ratio of 2.7). After 6 h on stream, 0 at% Nb 1 wt% Pt catalyst showed only Pt^0 species, while in the 25 at% Nb 1 wt% Pt catalyst the Pt$^{\delta+}$/Pt^0 ratio increased (Pt$^{\delta+}$/Pt^0 ratio of 4.4). Thus, the presented data demonstrated that the acidity modulation of the supports (due to the presence of Nb) led to significant changes in the MSI, affecting both the nature and dispersion of the metallic phase. Moreover, coke deposition on the catalysts' surface was evidenced by a 2.4-fold increase of the C at% content for 0 at% Nb 1 wt % Pt and 3.0-fold increase for the 25 at% Nb 1 wt% Pt, corroborating the results obtained through Raman spectroscopy (Fig. S10), TG analysis (Fig. S11), and catalytic performance (Fig. 6, S8, S9, S14, and S15).

To better address the structure-performance relationship of the Pt-supported catalysts, in situ CO-DRIFTS and CO-TPD measurements were conducted (Fig. S21) to get insight into differences in the metal electronic states and metal site geometry. The CO-DRFITS spectrum of reduced 0 at% Nb 1 wt% Pt catalyst (Fig. S21a) presented contributions at 2053 cm^{-1}, 2076 cm^{-1}, 2083 cm^{-1} (CO stretches associated with metallic Pt sites), and 2103 cm^{-1} (CO stretch associated with oxidized Pt sites). Lentz et al. [64] employed DFT calculations to investigate the impact of Pt particle size on the CO adsorption spectrum profile, in which they demonstrated that larger particles led to sharper and more blue-shifted peaks. These results are in agreement with experimental data of CO adsorption on Pt/Al$_2$O$_3$ catalysts with different Pt particle sizes [65]. The larger particle scenario (i.e. ~3.5 nm) investigated in the former work presented a spectrum profile similar to that observed for the 0 at% Nb 1 wt% Pt catalyst, demonstrating the predominance of
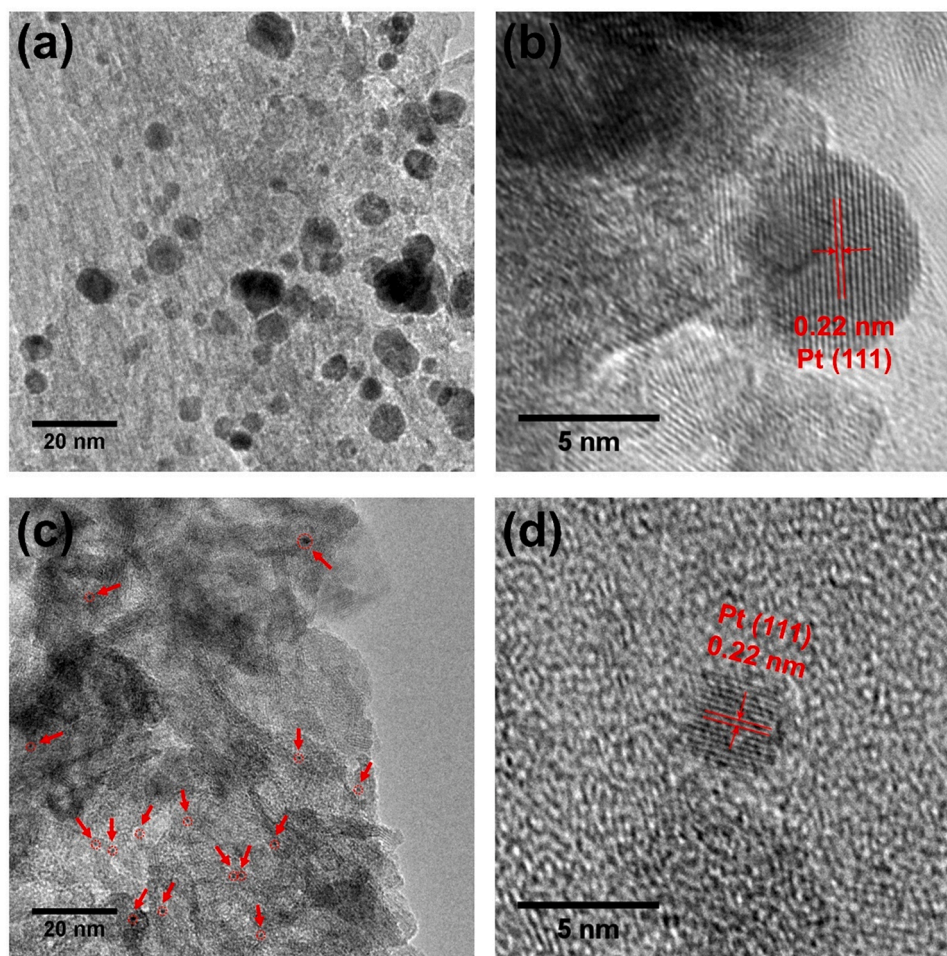
Fig. 7. TEM images of reduced (a-b) 0 at% Nb 1 wt% Pt and (c-d) 25 at% Nb 1 wt% Pt. Scale bars are presented within the figures.

large particles, which is in good agreement with TEM (Fig. 7 and S18) and XRD (Fig. S17) data. Pt {111} facets become more dominant as the particle size increases, leading to sharper peaks, as observed for the band centered at 2083 cm^{-1}, which could be associated with higher coordination metallic Pt sites at {111} facets. The absorption at 2076 cm^{-1} could be associated with similar sites, suggesting a broad size distribution of Pt particles, which was confirmed by TEM analysis (Fig. 7 and S18). While the absorption observed at 2053 cm^{-1} could be assigned to lower coordination metallic Pt sites, associated with edges, corners, and {100} facets sites [64,66,67]. The observed Pt electronic states are aligned with those observed through XPS data (Fig. 8), in which metallic Pt was dominant, while the absorption at 2103 cm^{-1} could be associated with Pt partially oxidized species. Additionally, the CO-TPD showed that the absorption bands associated with chemisorbed CO on Pt significantly decreased above 150 °C in this sample.

High-temperature reduction treatment is the most common method to construct SMSI, which is strongly related to the formation of oxygen vacancies, and their corresponding undercoordinated metal cations. Liu et. al [68] employed different reduction temperatures (i.e. 200, 350, and 450 °C) before CO adsorption experiments over Pt/TiO$_2$ systems, with Pt particle sizes similar to 0 at% Nb 1 wt% Pt catalyst. They demonstrated that the higher the reduction temperature, Pt sites became less available, which could be associated with partial and/or permeable TiO$_x$ overlayer encapsulation [69]. Wu et. al [70] observed the same effect after increasing the reduction temperature from 200 °C to 350 °C, for Pt/TiO$_2$ systems with different preferential TiO$_2$ exposed facets. Nevertheless, in both cases, Pt sites were still available after reduction at temperatures ≥ 350 °C. In this regard, we can not discard that SMSI effects are

occurring over 0 at% Nb 1 wt% Pt catalyst too. Thus, CO-uptake experiments were conducted, in which the 0 at% Nb 1 wt% Pt catalyst resulted in a dispersion of 6.7% and an average particle size of 16.6 nm. The estimated average particle size was 3.1-fold larger than that observed through TEM analysis (Fig. 7, S16, S18, and Table S7), corroborating that a partial and/or permeable TiO$_x$ overlayer encapsulation over the Pt particles occurred.

In the case of 25 at% Nb 1 wt% Pt catalyst (Fig. S21c), a single broad band ranging from about 2130 cm^{-1} to 2030 cm^{-1} was observed. The large width band suggests that CO molecules adsorbed on different geometrical sites of small particles (<1.5 nm), in which the orientation and bond length of CO molecules were slightly different at similar binding sites [64,65]. Therefore, a unique wavenumber cannot be assigned to a specific binding site on a small nanoparticle that is fully covered with CO. TEM (Fig. 7, S16, and S18) and XRD (Fig. S17) analyses confirmed the presence of small particles. Lentz et al. [64] calculated IR spectra of small particles (i.e. ~1.07 nm), which presented a broad band in a similar region to that observed for 25 at% Nb 1 wt% Pt catalyst, comprising {111} and {100} facets, corners, and edges sites. The wide wavenumber covered by this band suggests that CO adsorbed over both metallic and oxidized Pt sites, which agrees with the species observed through XPS (Fig. 8). CO-TPD measurements (Fig. S21c) demonstrated that by increasing the temperature the absorption bands related to CO chemisorbed over Pt sites became more intense and it led to an increase in the contributions at higher wavenumber, related to oxidized Pt sites. This phenomenon could be associated with a porous oxidic encapsulation overlayer due to the SMSI [69,71], in which the higher the temperature, the higher its permeability and availability of Pt
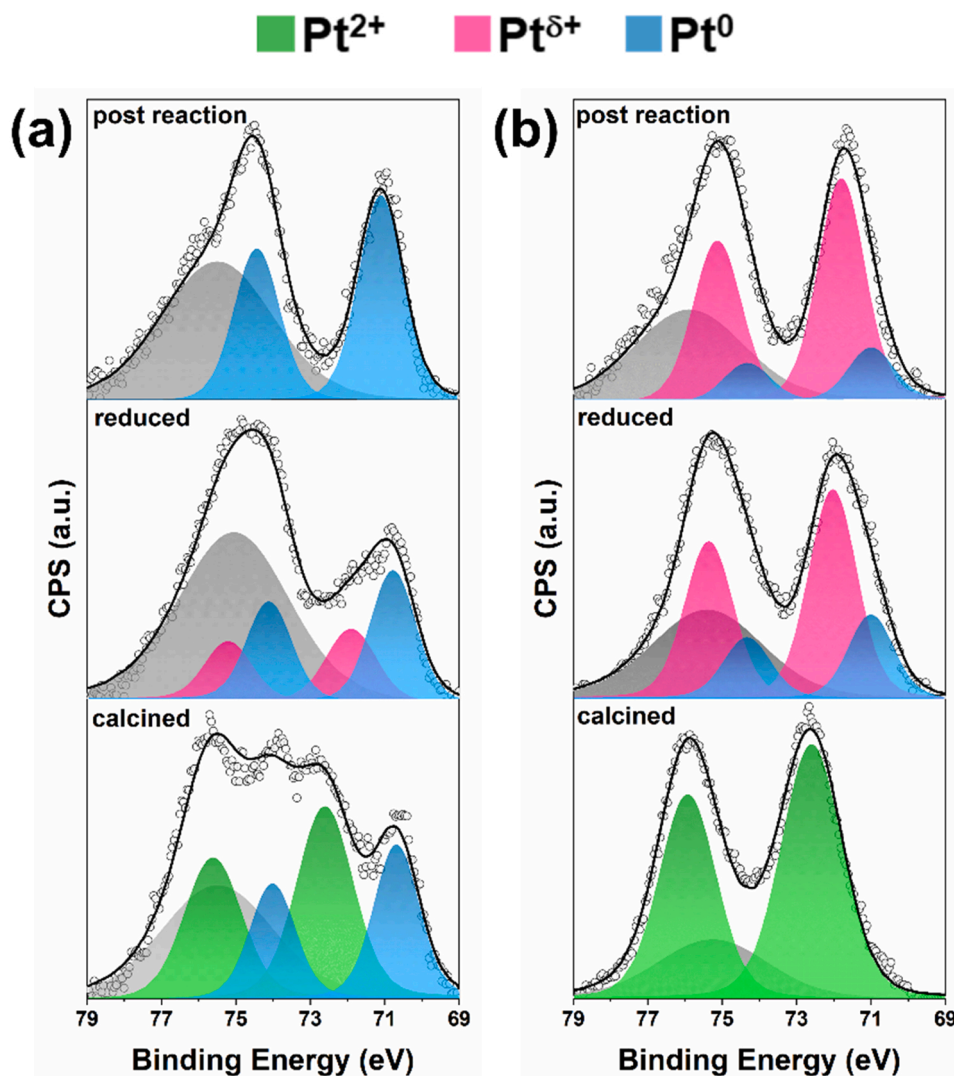
Fig. 8. XPS spectra of calcined, reduced (pre-reaction), and post-reaction catalysts of (a) 0 at% Nb 1 wt% Pt and (b) 25 at% Nb 1 wt% Pt. The nature of the Pt species is indicated by the colors above the graphics. The gray peak corresponds to the Ti 3 s satellite; see SI for details and Figs. S19,20.

sites. CO-uptake analysis resulted in a dispersion of 10.9% and an average particle size of 10.2 nm, which is 4-fold larger than that observed through TEM (Fig. 7, S16, S18, and Table S7), corroborating the formation of an oxidic overlayer. Additionally, by comparing the region associated with carbonates absorption (Figs. S21b,d), it was possible to notice that the carbonate species also differed between the catalysts.

Py-FTIR measurements were also conducted over the calcined and reduced Pt-supported catalysts (Fig. 9) to get insight into the acid site modifications upon metallic phase addition. For both supports, Pt impregnation led to the formation of a stronger Lewis acid contribution associated with a new band at 1454 cm^{-1}. The ratios between the strong (Ls) and weak (Lw) Lewis sites (values presented in Fig. 9) showed that the 25 at% Nb 1 wt% Pt catalysts were richer in strong Lewis acid sites. We assume that the Ls sites are associated with Ti^{3+} species formed in the vicinity of the metal/oxide interface, as locally demonstrated through EELS measurements of Ti $L_{2,3}$ edge in Pt/TiO$_2$ systems [62].

A decrease in Brønsted/Lewis acid site ratio also occurred after Pt impregnation for both supports (Table S8). Yang et al. [72] demonstrated that Brønsted acid sites were prone to the adsorption, stabilization, and dispersion of Pd species over ZrO$_2$, which they related to a Brønsted-SMSI effect. This same effect was also observed for Pd supported over H-ZSM-5 zeolite [73], and Pt or Pt/Re supported over USY

zeolite [74]. The Brønsted/Lewis acid site ratio decreased by more than a half in the calcined 25 at% Nb 1 wt% Pt catalyst compared to its bare support. Nevertheless, the total acidity was not affected (514 $\pm$ 23 μmol g^{-1} compared to 527 $\pm$ 22 μmol g^{-1} of the bare support). It indicates a decrease in Brønsted acid site concentration; thus, we believe that the Brønsted-SMSI effect could also be taking place for the catalysts employed in this work.

In summary, it was possible to understand how the Nb insertion into the TiO$_2$ matrix affects the catalytic performance in the acetone HDO reaction. For the bare supports, the high selectivity to C-C coupling reactions, leading to the formation of condensation products (Fig. 6a,b, and Fig. S7), could be associated with the prevalence of AS (381–602 μmol g^{-1}), regardless of their nature (Brønsted or Lewis). The addition of Pt led to HDO catalysts ruled by a bifunctional mechanism, resulting in selective C-O bond cleavage and high conversions and DODs in the initial hours on stream (Fig. 6c,d,e). However, the evolution of products distribution over TOS was significantly affected depending on the support (i.e., 0 at% Nb and 25 at% Nb). The presence of Nb and the modulation of the acidity affected both the nature and dispersion of the metallic phase (Figs. 7,8 and Table S5), and consequently, it also impacted the creation of interfacial sites and their oxophilicity. The 0 at % Nb 1 wt% Pt catalyst led to the formation of larger Pt particles and the predominance of Pt^0 species, which were highly susceptible to coke
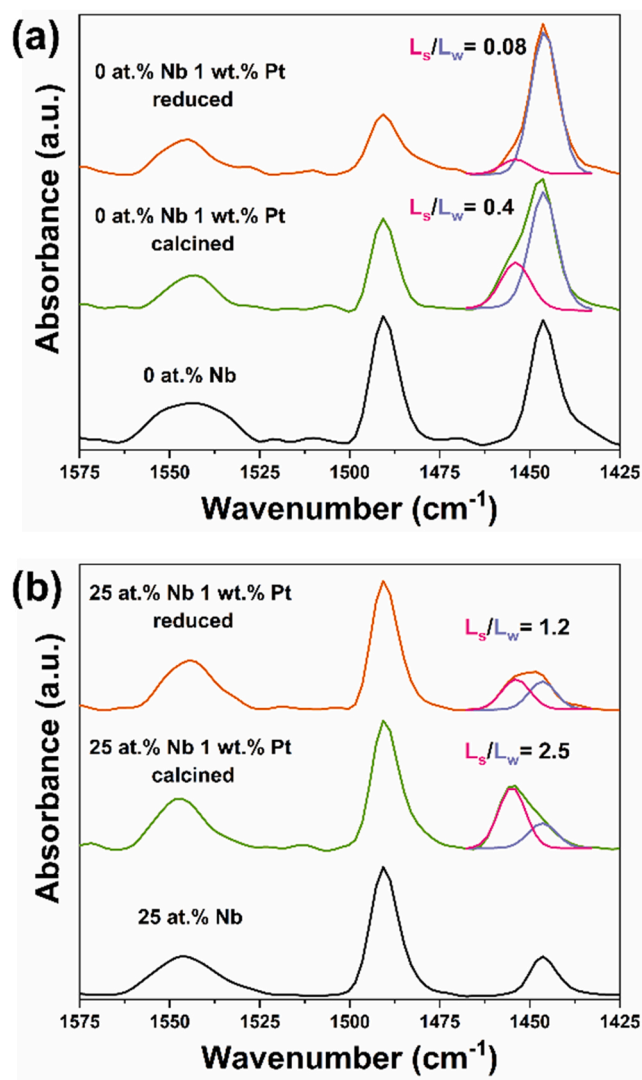
Fig. 9. Py-FTIR of (a) bare 0 at% Nb (calcined) and 0 at% Nb 1 wt% Pt calcined and reduced; (b) bare 25 at% Nb (calcined) and 25 at% Nb 1 wt% Pt calcined and reduced. L_s stands for strong Lewis acid sites, and L_w for weak Lewis acid sites.

deposition [75,76]. The catalytic performance over TOS demonstrated the fast deactivation of the MS (TOS < 6 h) and prevalence of AS (TOS > 6 h), where condensation products represented about 83% of the total products at the end of 20 h on stream (Fig. 6c). On the other hand, in the 25 at% Nb 1 wt% Pt catalyst, the Pt dispersion was enhanced, and $Pt^{\delta+}$ species prevailed, decreasing the coke deposition rate over the MS and resulting in more stable MS. In addition, the more electron-deficient $Pt^{\delta+}$ sites had limited hydrogenation capability, here favoring the formation of propylene rather than propane. Therefore, we can conclude that the acidity modulation introduced by Nb addition into the TiO_2 lattice changed the MSI, where the oxide richer in Brønsted acid sites (total concentration of Brønsted acid sites of 378 μmol g^{-1}), i.e., 25 at% Nb, resulted in more oxidized and dispersed Pt particles, which we believe can be associated with the Brønsted-SMSI effect. Although the nature and modulation of Brønsted/Lewis acid sites did not significantly impact the selectivity over acetone HDO products, it can impact ongoing research in other reactions that are more sensitive to these variations.

4. Conclusions

Morphological and structural modifications were verified upon Nb

insertion into the TiO_2 anatase crystal lattice, according to SEM, XRD, and short- and medium-range order PDF analysis. Acidity modulation of Ti-Nb mixed metal oxides was accomplished by employing different Ti: Nb proportions; it was demonstrated that Brønsted/Lewis acid sites ratio increased along with the Nb content up to 25% at%. Acid site distribution per accessible area revealed that all mixed oxides presented similar values, between 0.84 and 1.18 sites per nm^2. By supporting the metallic phase in the mixed oxide with higher B/L ratio (25 at% Nb), the DOD was kept over 55% along 20 h on stream, while the catalyst based on the support with lower B/L ratio (0 at% Nb) led to a DOD more than 3 times smaller. XPS measurements of pre- and post-reaction Pt-supported catalysts indicated that the Pt dispersion and its species differed depending on the employed support. Pt-supported on 25 at% Nb led to more oxidized Pt species than on 0 at% Nb, in addition to a better dispersion. More oxidized Pt species led to less extensive coke deposition, resulting in more stable metallic sites.

The presented catalytic performance demonstrated that Pt-supported catalysts with selective C-O bond cleavage could be designed through the modulation of catalytic sites of the support. We also showed that the acidity modulation of the support could lead to significant changes in the MSI, affecting both the nature and stability of the catalytic sites. Thus, here we established a better understanding of the correlation between acidity and MSI effects of Pt-supported over metal oxides, along with a correlation of these properties with the catalytic performance. We expect that the presented data can give important insights into developing promising catalytic systems for HDO reactions.

CRediT authorship contribution statement

G. B. Strapasson: Conceptualization, Investigation, Methodology, Validation, Data curation, Visualization, Writing – original draft. **L. S. Sousa:** Investigation, Methodology, Data curation, Writing – original draft. **G. B. Báfero:** Investigation, Methodology, Data curation, Writing – original draft. **D. S. Leite:** Investigation, Methodology, Data curation, Writing – original draft. **B. D. Moreno:** Investigation, Methodology. **C. B. Rodella:** Conceptualization, Supervision, Writing – review & editing, Project administration, Funding acquisition. **D. Zanchet:** Conceptualization, Supervision, Writing – review & editing, Project administration, Funding acquisition.

Declaration of Competing Interest

The authors declare that they have no known competing financial interests or personal relationships that could have appeared to influence the work reported in this paper.

Data Availability

Data will be made available on request.

Acknowledgments

LNNano, CNPEM, CINE, and CLS staff for their support. L.M. Rossi group is acknowledged for the access and support during the CO chemisorption uptake experiments.

Appendix A. Supporting information

Supplementary data associated with this article can be found in the online version at doi:10.1016/j.apcatb.2023.122863.

References

[1] T. Prasomsri, T. Nimmanwudipong, Y. Román-Leshkov, Effective hydrodeoxygenation of biomass-derived oxygenates into unsaturated hydrocarbons by MoO_3 using low H_2 pressures, Energy Environ. Sci. 6 (2013) 1732–1738, https://doi.org/10.1039/c3ee24360e.

[2] C.A. Teles, R.C. Rabelo-Neto, J.R. de Lima, L.V. Mattos, D.E. Resasco, F.B. Noronha, The effect of metal type on hydrodeoxygenation of phenol over silica supported catalysts, Catal. Lett. 146 (2016) 1848–1857, https://doi.org/10.1007/s10562-016-1815-5.

[3] Y.S. Yun, C.E. Berdugo-Díaz, D.W. Flaherty, Advances in understanding the selective hydrogenolysis of biomass derivatives, ACS Catal. 11 (2021) 11193–11232, https://doi.org/10.1021/acscatal.1c02866.

[4] W. Zhang, Y. Zhang, L. Zhao, W. Wei, Catalytic activities of NiMo carbide supported on SiO_2 for the hydrodeoxygenation of ethyl benzoate, acetone, and acetaldehyde, Energy Fuels 24 (2010) 2052–2059, https://doi.org/10.1021/ef901222z.

[5] J. Sun, R.A.L. Baylon, C. Liu, D. Mei, K.J. Martin, P. Venkitasubramanian, Y. Wang, Key roles of lewis acid-base pairs on $Zn_xZr_yO_z$ in direct ethanol/acetone to isobutene conversion, J. Am. Chem. Soc. 138 (2016) 507–517, https://doi.org/10.1021/jacs.5b07401.

[6] Y. Lykhach, F. Faisal, T. Skála, A. Neitzel, N. Tsud, M. Vorokhta, F. Dvořák, K. Beranová, Y. Kosto, K.C. Prince, V. Matolín, J. Libuda, Interplay between the metal-support interaction and stability in $Pt/Co_3O_4(111)$ model catalysts, J. Mater. Chem. A 6 (2018) 23078–23086, https://doi.org/10.1039/c8ta08142e.

[7] T.W. van Deelen, C. Hernández Mejía, K.P. de Jong, Control of metal-support interactions in heterogeneous catalysts to enhance activity and selectivity, Nat. Catal. 2 (2019) 955–970, https://doi.org/10.1038/s41929-019-0364-x.

[8] Z. Wang, C. Wang, S. Mao, B. Lu, Y. Chen, X. Zhang, Z. Chen, Y. Wang, Decoupling the electronic and geometric effects of Pt catalysts in selective hydrogenation reaction, Nat. Commun. 13 (2022) 1–10, https://doi.org/10.1038/s41467-022-31313-4.

[9] J. Goscianska, M. Ziolek, E. Gibson, M. Daturi, Meso-macroporous zirconia modified with niobia as support for platinum - Acidic and basic properties, Catal. Today 152 (2010) 33–41, https://doi.org/10.1016/j.cattod.2009.10.016.

[10] A. Hervier, L.R. Baker, K. Komvopoulos, G.A. Somorjai, Titanium oxide/platinum catalysis: Charge transfer from a titanium oxide support controls activity and selectivity in methanol oxidation on platinum, J. Phys. Chem. C 115 (2011) 22960–22964, https://doi.org/10.1021/jp2066327.

[11] A. Beck, X. Huang, L. Artiglia, M. Zabilskiy, X. Wang, P. Rzepka, D. Palagin, M. G. Willinger, J.A. van Bokhoven, The dynamics of overlayer formation on catalyst nanoparticles and strong metal-support interaction, Nat. Commun. 11 (2020) 1–8, https://doi.org/10.1038/s41467-020-17070-2.

[12] W. Zhao, D. Zhou, S. Han, Y. Li, J. Liu, Y. Zhou, M. Li, X. Zhang, W. Shen, Metal-support interaction in Pt/TiO_2: formation of surface Pt-Ti alloy, J. Phys. Chem. C. 125 (2021) 10386–10396, https://doi.org/10.1021/acs.jpcc.1c02108.

[13] P. Schlexer, D. Widmann, R.J. Behm, G. Pacchioni, CO oxidation on a Au/TiO_2 nanoparticle catalyst via the Au-assisted mars-van krevelen mechanism, ACS Catal. 8 (2018) 6513–6525, https://doi.org/10.1021/acscatal.8b01751.

[14] S. Bagheri, N. Muhd Julkapli, S. Bee Abd Hamid, Titanium dioxide as a catalyst support in heterogeneous catalysis, Sci. World J. (2014) (2014), https://doi.org/10.1155/2014/727496.

[15] V.I. Sobolev, L.V. Pirutko, Room temperature reduction of N_2O by CO over Au/TiO_2, Catal. Commun. 18 (2012) 147–150, https://doi.org/10.1016/j.catcom.2011.11.034.

[16] E. Wada, M. Kitano, K. Yamamoto, K. Nakajima, S. Hayashi, M. Hara, Synthesis of niobium-doped titanate nanotubes as solid acid catalysts, Catal. Sci. Technol. 6 (2016) 4832–4839, https://doi.org/10.1039/c6cy00044d.

[17] L.F. da Silva, W. Avansi, A.C. Catto, J.E.F.S. Rodrigues, M.I.B. Bernardi, V. R. Mastelaro, The role of Nb addition in TiO_2 nanoparticles: phase transition and photocatalytic properties, Phys. Status Solidi Appl. Mater. Sci. 215 (2018) 1800321, https://doi.org/10.1002/pssa.201800321.

[18] A. Takagaki, T. Yoshida, D. Lu, J.N. Kondo, M. Hara, K. Domen, S. Hayashi, Titanium niobate and titanium tantalate nanosheets as strong solid acid catalysts, J. Phys. Chem. B 108 (2004) 11549–11555, https://doi.org/10.1021/jp049170e.

[19] A. Takagaki, C. Tagusagawa, S. Hayashi, M. Hara, K. Domen, Nanosheets as highly active solid acid catalysts for green chemical syntheses, Energy Environ. Sci. 3 (2010) 82–93, https://doi.org/10.1039/b918563a.

[20] G.S. Foo, D. Wei, D.S. Sholl, C. Sievers, Role of Lewis and brønsted acid sites in the dehydration of glycerol over niobia, ACS Catal. 4 (2014) 3180–3192, https://doi.org/10.1021/cs5006376.

[21] W. Liu, W. Zhang, M. Liu, P. Du, C. Dang, J. Liang, Y. Li, Fabrication of niobium doped titanate nanoflakes with enhanced visible-light-driven photocatalytic

[22] L.M. Nikolić, M. Milanović, S. Nedić, K. Giannakopoulos, A.G. Kontos, Hydrothermal conversion of Nb-anatase nanoparticles into layered titanates, Ceram. Int. 37 (2011) 111–117, https://doi.org/10.1016/j.ceramint.2010.08.022.

[23] N. Duong, Q. Tan, D.E. Resasco, Controlling phenolic hydrodeoxygenation by tailoring metal–O bond strength via specific catalyst metal type and particle size selection, Comptes Rendus Chim. 21 (2018) 155–163, https://doi.org/10.1016/j.crci.2017.07.008.

[24] C.A. Teles, P.M. de Souza, R.C. Rabelo-Neto, M.B. Griffin, C. Mukarakate, K. A. Orton, D.E. Resasco, F.B. Noronha, Catalytic upgrading of biomass pyrolysis vapors and model compounds using niobia supported Pd catalyst, Appl. Catal. B Environ. 238 (2018) 38–50, https://doi.org/10.1016/j.apcatb.2018.06.073.

[25] P.M. De Souza, R.C. Rabelo-Neto, L.E.P. Borges, G. Jacobs, B.H. Davis, T. Sooknoi, D.E. Resasco, F.B. Noronha, Role of keto intermediates in the hydrodeoxygenation of phenol over Pd on oxophilic supports, ACS Catal. 5 (2015) 1318–1329, https://doi.org/10.1021/cs501853t.

[26] M. Lu, H. Du, B. Wei, J. Zhu, M. Li, Y. Shan, C. Song, Catalytic hydrodeoxygenation of guaiacol over palladium catalyst on different titania supports, Energy Fuels 31 (2017) 10858–10865, https://doi.org/10.1021/acs.energyfuels.7b01498.

[27] M. Shetty, K. Murugappan, T. Prasomsri, W.H. Green, Y. Román-Leshkov, Reactivity and stability investigation of supported molybdenum oxide catalysts for the hydrodeoxygenation (HDO) of m-cresol, J. Catal. 331 (2015) 86–97, https://doi.org/10.1016/j.jcat.2015.07.034.

[28] C.A. Teles, R.C. Rabelo-Neto, N. Duong, J. Quiroz, P.H.C. Camargo, G. Jacobs, D. E. Resasco, F.B. Noronha, Role of the metal-support interface in the hydrodeoxygenation reaction of phenol, Appl. Catal. B Environ. 277 (2020), https://doi.org/10.1016/j.apcatb.2020.119238.

[29] D.L. Morgan, H.W. Liu, R.L. Frost, E.R. Waclawik, Implications of precursor chemistry on the alkaline hydrothermal synthesis of Titania/Titanate nanostructures, J. Phys. Chem. C. 114 (2010) 101–110, https://doi.org/10.1021/jp908508z.

[30] N. Liu, X. Chen, J. Zhang, J.W. Schwank, A review on TiO_2-based nanotubes synthesized via hydrothermal method: formation mechanism, structure modification, and photocatalytic applications, Catal. Today 225 (2014) 34–51, https://doi.org/10.1016/j.cattod.2013.10.090.

[31] P. Roy, S. Berger, P. Schmuki, TiO_2 nanotubes: synthesis and applications, Angew. Chem. - Int. Ed. 50 (2011) 2904–2939, https://doi.org/10.1002/anie.201001374.

[32] D.S. Leite, G.B. Strapasson, D. Zanchet, Unveiling the effect of metallic and oxidized phases of cobalt on acetone hydrodeoxygenation, Mol. Catal. 530 (2022), 112623, https://doi.org/10.1016/j.mcat.2022.112623.

[33] M. Milanović, L.M. Nikolić, I. Stijepović, A.G. Kontos, K.P. Giannakopoulos, Steps in growth of Nb-doped layered titanates with very high surface area suitable for water purification, Mater. Chem. Phys. 148 (2014) 874–881, https://doi.org/10.1016/j.matchemphys.2014.08.064.

[34] T. Egami, S.J.L. Billinge, Underneath the Bragg Peaks: Structural Analysis of Complex Materials, 2nd Edition, 2012.

[35] T.L. Christiansen, S.R. Cooper, K.M.O. Jensen, There's no place like real-space: elucidating size-dependent atomic structure of nanomaterials using pair distribution function analysis, Nanoscale Adv. 2 (2020) 2234–2254, https://doi.org/10.1039/d0na00120a.

[36] A. Mancini, L. Malavasi, S.J.L. Billinge, M.F. Thorpe, Recent advances in the application of total scattering methods to functional materials, Kluwer Academic Publishers, New York, 2015, https://doi.org/10.1039/c5cc07429k.

[37] W. Ji, N. Wang, Q. Li, H. Zhu, K. Lin, J. Deng, J. Chen, H. Zhang, X. Xing, Oxygen vacancy distributions and electron localization in a $CeO2(100)$ nanocube, Inorg. Chem. Front. 9 (2022) 275–283, https://doi.org/10.1039/d1qi01179k.

[38] V.P. Pakharukova, D.I. Potemkin, O.A. Stonkus, N.A. Kharchenko, A.A. Saraev, A. M. Gorlova, Investigation of the structure and interface features of $Ni/Ce_{1-x}Zr_xO_2$ catalysts for CO and CO_2 methanation, J. Phys. Chem. C. 125 (2021) 20538–20550, https://doi.org/10.1021/acs.jpcc.1c05529.

[39] C.I. Hiley, H.Y. Playford, J.M. Fisher, N.C. Felix, D. Thompsett, R.J. Kashtiban, R. I. Walton, Pair distribution function analysis of structural disorder by Nb^{5+} inclusion in ceria: evidence for enhanced oxygen storage capacity from under-coordinated oxide, J. Am. Chem. Soc. 140 (2018) 1588–1591, https://doi.org/10.1021/jacs.7b12421.

[40] M.C. Biesinger, B.P. Payne, B.R. Hart, A.P. Grosvenor, N.S. McIntyre, L.W.M. Lau, R.S.C. Smart, Quantitative chemical state XPS analysis of first row transition metals, oxides and hydroxides, J. Phys. Conf. Ser. 100 (2008), https://doi.org/10.1088/1742-6596/100/1/012025.

[41] J.F. Moulder, W.F. Stickle, P.E. Sobol, K.D. Bomben, Handbook of X-ray photoelectron spectroscopy: a reference book of standard spectra for identification and interpretation of xps data, perkin-elmer corporation, Phys. Electron. Div., Minn., USA (1992).

[42] J. Liu, R. tang Guo, Z. zhen Guan, X. Sun, W. guo Pan, X. yu Liu, Z. yi Wang, X. Shi, H. Qin, Z. zhu Qiu, S. wei Liu, Simultaneous removal of NO and Hg^0 over Nb-Modified $MnTiO_x$ catalyst, Int. J. Hydrog. Energy 44 (2019) 835–843, https://doi.org/10.1016/j.ijhydene.2018.11.006.

[43] A. Sharma, U. Bhardwaj, D. Jain, H.S. Kushwaha, $NaNbO_3$ nanorods: photopiezocatalysts for elevated bacterial disinfection and wastewater treatment, ACS Omega 7 (2022) 7595–7605, https://doi.org/10.1021/acsomega.1c06109.

[44] A. Corma, Inorganic solid acids and their use in acid-catalyzed hydrocarbon reactions, Chem. Rev. 95 (1995) 559–614, https://doi.org/10.1021/cr00035a006.

[45] M. Tamura, K.I. Shimizu, A. Satsuma, Comprehensive IR study on acid/base properties of metal oxides, Appl. Catal. A Gen. 433–434 (2012) 135–145, https://doi.org/10.1016/j.apcata.2012.05.008.

[46] C.A. Emeis, Determination of integrated molar extinction coefficients for ir absorption bands of pyridine adsorbed on solid acid catalysts, J. Catal. 141 (1993) 347–354, https://doi.org/10.1006/jcat.1993.1145.

[47] M. Luisa Marin, G.L. Hallett-Tapley, S. Impellizzeri, C. Fasciani, S. Simoncelli, J. C. Netto-Ferreira, J.C. Scaiano, Synthesis, acid properties and catalysis by niobium oxide nanostructured materials, Catal. Sci. Technol. 4 (2014) 3044–3052, https://doi.org/10.1039/c4cy00238e.

[48] I. Nowak, M. Ziolek, Niobium compounds: preparation, characterization, and application in heterogeneous catalysis, Chem. Rev. 99 (1999) 3603–3624, https://doi.org/10.1021/cr9800208.

[49] K. Nakajima, Y. Baba, R. Noma, M. Kitano, J.N. Kondo, S. Hayashi, M. Hara, $Nb_2O_5 \bullet nH_2O$ as a heterogeneous catalyst with water-tolerant lewis acid sites, J. Am. Chem. Soc. 133 (2011) 4224–4227, https://doi.org/10.1021/ja110482r.

[50] A. Zheng, F. Deng, S. Bin Liu, Acidity Characterization of Solid Acid Catalysts by Solid-State ^{31}P NMR of Adsorbed Phosphorus-Containing Probe Molecules, 1st ed., Elsevier Ltd, 2014 https://doi.org/10.1016/B978-0-12-800185-1.00002-4.

[51] A. Zheng, S. Li, S Bin Liu, F. Deng, Acidic properties and structure-activity correlations of solid acid catalysts revealed by solid-state NMR spectroscopy, Acc. Chem. Res. 49 (2016) 655–663, https://doi.org/10.1021/acs.accounts.6b00007.

[52] X. Yi, H.H. Ko, F. Deng, S. Bin Liu, A. Zheng, Solid-state ^{31}P NMR mapping of active centers and relevant spatial correlations in solid acid catalysts, Nat. Protoc. 15 (2020) 3527–3555, https://doi.org/10.1038/s41596-020-0385-6.

[53] A. Zheng, S. Bin Liu, F. Deng, ^{31}P NMR chemical shifts of phosphorus probes as reliable and practical acidity scales for solid and liquid catalysts, Chem. Rev. 117 (2017) 12475–12531, https://doi.org/10.1021/acs.chemrev.7b00289.

[54] M. Kitano, E. Wada, K. Nakajima, S. Hayashi, S. Miyazaki, H. Kobayashi, M. Hara, Protonated titanate nanotubes with Lewis and Brønsted acidity: Relationship between nanotube structure and catalytic activity, Chem. Mater. 25 (2013) 385–393, https://doi.org/10.1021/cm303324b.

[55] S. Lang, M. Benz, U. Obenaus, R. Himmelmann, M. Hunger, Novel approach for the characterization of lewis acidic solid catalysts by solid-state NMR spectroscopy, ChemCatChem 8 (2016) 2031–2036, https://doi.org/10.1002/cctc.201600372.

[56] P.V. Wiper, J. Amelse, L. Mafra, Multinuclear solid-state NMR characterization of the Brønsted/Lewis acid properties in the BP HAMS-1B (H-[B]-ZSM-5) borosilicate molecular sieve using adsorbed TMPO and TBPO probe molecules, J. Catal. 316 (2014) 240–250, https://doi.org/10.1016/j.jcat.2014.05.017.

[57] C.P. Nash, A. Ramanathan, D.A. Ruddy, M. Behl, E. Gjersing, M. Griffin, H. Zhu, B. Subramaniam, J.A. Schaidle, J.E. Hensley, Mixed alcohol dehydration over Brønsted and Lewis acidic catalysts, Appl. Catal. A Gen. 510 (2016) 110–124, https://doi.org/10.1016/j.apcata.2015.11.019.

[58] H. Li, D. Guo, N. Ulumuddin, N.R. Jaegers, J. Sun, B. Peng, J.-S. McEwen, J. Hu, Y. Wang, Elucidating the cooperative roles of water and lewis acid–base pairs in cascade C–C coupling and self-deoxygenation reactions, JACS Au 1 (2021) 1471–1487, https://doi.org/10.1021/jacsau.1c00218.

[59] S. Herrmann, E. Iglesia, Selective conversion of acetone to isobutene and acetic acid on aluminosilicates: Kinetic coupling between acid-catalyzed and radical-mediated pathways, J. Catal. 360 (2018) 66–80, https://doi.org/10.1016/j.jcat.2018.01.032.

[60] J. Sun, A.M. Karim, H. Zhang, L. Kovarik, X.S. Li, A.J. Hensley, J.S. McEwen, Y. Wang, Carbon-supported bimetallic Pd-Fe catalysts for vapor-phase hydrodeoxygenation of guaiacol, J. Catal. 306 (2013) 47–57, https://doi.org/10.1016/j.jcat.2013.05.020.

[61] J. He, C. Zhao, J.A. Lercher, Impact of solvent for individual steps of phenol hydrodeoxygenation with Pd/C and HZSM-5 as catalysts, J. Catal. 309 (2014) 362–375, https://doi.org/10.1016/j.jcat.2013.09.009.

[62] M. Chen, W. Wang, Y. Qiu, H. Wen, G. Li, Z. Yang, P. Wang, Identification of active sites in HCHO oxidation over TiO_2-supported Pt catalysts, ACS Catal. 12 (2022) 5565–5573, https://doi.org/10.1021/acscatal.2c01150.

[63] T. Huizinga, J. Van Grondelle, R. Prins, A temperature programmed reduction study of Pt on Al_2O_3 and TiO_2, Appl. Catal. 10 (1984) 199–213, https://doi.org/10.1016/0166-9834(84)80104-9.

[64] C. Lentz, S.P. Jand, J. Melke, C. Roth, P. Kaghazchi, DRIFTS study of CO adsorption on Pt nanoparticles supported by DFT calculations, J. Mol. Catal. A Chem. 426 (2017) 1–9, https://doi.org/10.1016/j.molcata.2016.10.002.

[65] A.D. Allian, K. Takanabe, K.L. Fujdala, X. Hao, T.J. Truex, J. Cai, C. Buda, M. Neurock, E. Iglesia, Chemisorption of CO and mechanism of CO oxidation on supported platinum nanoclusters, J. Am. Chem. Soc. 133 (2011) 4498–4517, https://doi.org/10.1021/ja110073u.

[66] L. DeRita, S. Dai, K. Lopez-Zepeda, N. Pham, G.W. Graham, X. Pan, P. Christopher, Catalyst architecture for stable single atom dispersion enables site-specific spectroscopic and reactivity measurements of CO adsorbed to Pt Atoms, oxidized Pt clusters, and metallic Pt clusters on TiO_2, J. Am. Chem. Soc. 139 (2017) 14150–14165, https://doi.org/10.1021/jacs.7b07093.

[67] H.V. Thang, G. Pacchioni, L. DeRita, P. Christopher, Nature of stable single atom Pt catalysts dispersed on anatase TiO_2, J. Catal. 367 (2018) 104–114, https://doi.org/10.1016/j.jcat.2018.08.025.

[68] X. Liu, Y. Ren, M. Wang, X. Ren, J. Liu, Q. Yang, Cooperation of Pt and TiO_x in the hydrogenation of nitrobenzothiazole, ACS Catal. 12 (2022) 11369–11379, https://doi.org/10.1021/acscatal.2c02988.

[69] Z. Luo, G. Zhao, H. Pan, W. Sun, Strong metal–support interaction in heterogeneous catalysts, Adv. Energy Mater. 12 (2022) 1–15, https://doi.org/10.1002/aenm.202201395.

[70] X. Wu, C. jun Liu, H. Wang, Q. Ge, X. Zhu, Origin of strong metal-support interactions between Pt and anatase TiO_2 facets for hydrodeoxygenation of m-cresol on Pt/TiO_2 catalysts, J. Catal. 418 (2023) 203–215, https://doi.org/10.1016/j.jcat.2023.01.023.

[71] S. Liu, H. Qi, J. Zhou, W. Xu, Y. Niu, B. Zhang, Y. Zhao, W. Liu, Z. Ao, Z. Kuang, L. Li, M. Wang, J. Wang, Encapsulation of platinum by titania under an oxidative atmosphere: contrary to classical strong metal-support interactions, ACS Catal. 11 (2021) 6081–6090, https://doi.org/10.1021/acscatal.1c01347.

[72] X. Yang, X. Ma, X. Yu, M. Ge, Exploration of strong metal-support interaction in zirconia supported catalysts for toluene oxidation, Appl. Catal. B Environ. 263 (2020), 118355, https://doi.org/10.1016/j.apcatb.2019.118355.

[73] Y. Lou, J. Ma, W. Hu, Q. Dai, L. Wang, W. Zhan, Y. Guo, X.M. Cao, Y. Guo, P. Hu, G. Lu, Low-temperature methane combustion over Pd/H-ZSM-5: active Pd sites with specific electronic properties modulated by acidic sites of H-ZSM-5, ACS Catal. 6 (2016) 8127–8139, https://doi.org/10.1021/acscatal.6b01801.

[74] K. Lee, M.E. Lee, J.K. Kim, B. Shin, M. Choi, Single-step hydroconversion of triglycerides into biojet fuel using CO-tolerant PtRe catalyst supported on USY, J. Catal. 379 (2019) 180–190, https://doi.org/10.1016/j.jcat.2019.09.043.

[75] Z. Peng, F. Somodi, S. Helveg, C. Kisielowski, P. Specht, A.T. Bell, High-resolution in situ and ex situ TEM studies on graphene formation and growth on Pt nanoparticles, J. Catal. 286 (2012) 22–29, https://doi.org/10.1016/j.jcat.2011.10.008.

[76] J. Wu, S. Helveg, S. Ullmann, Z. Peng, A.T. Bell, Growth of encapsulating carbon on supported Pt nanoparticles studied by in situ TEM, J. Catal. 338 (2016) 295–304, https://doi.org/10.1016/j.jcat.2016.03.010.